JOURNAL OF AIRCRAFT
Vol. 47, No. 4, July–August 2010

In Pursuit of Grid Convergence for Two-Dimensional Euler Solutions

John C. Vassberg*
The Boeing Company, Huntington Beach, California 92647
and
Antony Jameson†
Stanford University, Stanford, California 94305

DOI: 10.2514/1.46737

Grid-convergence trends of two-dimensional Euler solutions are investigated. The airfoil geometry under study is based on the NACA0012 equation. However, unlike the NACA0012 airfoil, which has a blunt base at the trailing edge, the study geometry is extended in chord so that its trailing edge is sharp. The flow solutions use extremely- high-quality grids that are developed with the aid of the Karman–Trefftz conformal transformation. The topology of each grid is that of a standard O-mesh. The grids naturally extend to a far-field boundary approximately 150 chord lengths away from the airfoil. Each quadrilateral cell of the resulting mesh has an aspect ratio of one. The intersecting lines of the grid are essentially orthogonal at each vertex within the mesh. A family of grids is recursively derived starting with the finest mesh. Here, each successively coarser grid in the sequence is constructed by eliminating every other node of the current grid, in both computational directions. In all, a total of eight grids comprise the family, with the coarsest-to-finest meshes having dimensions of 32 × 32–4096 × 4096 cells, respectively. Note that the finest grid in this family is composed of over 16 million cells, and is suitable for 13 levels of multigrid. The geometry and grids are all numerically defined such that they are exactly symmetrical about the horizontal axis to ensure that a nonlifting solution is possible at zero degrees angle-of-attack attitude. Characteristics of three well-known flow solvers (FLO82, OVERFLOW, and CFL3D) are studied using a matrix of four flow conditions: (subcritical and transonic) by (nonlifting and lifting). The matrix allows the ability to investigate grid-convergence trends of 1) drag with and without lifting effects, 2) drag with and without shocks, and 3) lift and moment at constant angles-of-attack. Results presented herein use 64-bit computations and are converged to machine-level-zero residuals. All three of the flow solvers have difficulty meeting this requirement on the finest meshes, especially at the transonic flow conditions. Some unexpected results are also discussed. Take for example the subcritical cases. FLO82 solutions do not reach asymptotic grid convergence of second-order accuracy until the mesh approaches one quarter of a million cells. OVERFLOW exhibits at best a first-order accuracy for a central-difference stencil. CFL3D shows second-order accuracy for drag, but only first-order trends for lift and pitching moment. For the transonic cases, the order of accuracy deteriorates for all of the methods. A comparison of the limiting values of the aerodynamic coefficients is provided. Drag for the subcritical cases nearly approach zero for all of the computational fluid dynamics methods reviewed. These and other results are discussed.

Nomenclature

C_d	=	drag coefficient $\frac{\text{drag}}{q_\infty C_{\text{ref}}}$
C_l	=	lift coefficient $\frac{\text{lift}}{q_\infty C_{\text{ref}}}$
C_m	=	pitching-moment coefficient
C_P	=	pressure coefficient $\frac{P-P_\infty}{q_\infty}$
C_{ref}	=	airfoil reference chord 1.0
count	=	drag coefficient unit 0.0001
ϵ	=	error of functional
$\mathcal{F}$	=	functional C_l, C_d, C_m
f, m, c	=	fine, medium, coarse meshes
$\mathcal{G}$	=	Newton-method function
h	=	cell size
i	=	grid index, circling the airfoil
j	=	grid index, airfoil to far field
LE	=	airfoil leading edge
M	=	Mach number $\frac{V}{a}$
NC	=	number of cells in one direction
P	=	power of Karman–Trefftz mapping
p	=	order of accuracy
q	=	dynamic pressure $\frac{1}{2}\rho V^2$
r	=	radial coordinate
R	=	radius of a circle
$\mathcal{R}$	=	ratio of grid-convergence deltas
TE	=	airfoil trailing edge
t	=	thickness of an airfoil
V	=	velocity
X_{ref}	=	moment reference center =0.25
x	=	horizontal physical coordinate
y	=	vertical physical coordinate
z	=	physical plane $z = x + iy$
α	=	angle of attack
β	=	normalized error parameter
ζ	=	mapped plane $\zeta = \xi + i\eta = re^{i\theta}$
η	=	vertical mapped coordinate
θ	=	angular coordinate
ξ	=	horizontal mapped coordinate
ρ	=	radius of curvature
τ	=	trailing-edge included angle
∞	=	signifies freestream conditions

Presented as Paper 2009-4114 at the 27th AIAA Applied Aerodynamics Conference, San Antonio, TX, 22–25 June 2009; received 14 August 2009; revision received 24 November 2009; accepted for publication 21 December 2009.

*Boeing Research and Technology, Boeing Technical Fellow. Fellow AIAA.

†Department of Aeronautics and Astronautics, Thomas V. Jones Professor of Engineering. Fellow AIAA.

I. Introduction

IN RECENT years, the AIAA computational fluid dynamics (CFD) Drag Prediction Workshop (DPW) Series [1] has drawn much attention to state-of-the-art CFD as a tool for accurate aerodynamic performance assessments of aircraft, especially in the transonic-flight regime. More specifically, the DPW Series has focused on CFD methods based on the Reynolds-averaged Navier–Stokes (RANS) equations, and on test cases concerned with predominantly turbulent high-Reynolds-number flows. The second and third workshops (DPW-II and DPW-III) have included grid-convergence studies. These investigations have yielded mixed results. As a consequence, there may be a need for the CFD community to pause for a moment and take a fresh look at the topic of grid convergence. To understand the issues contributing to the grid-convergence results documented by the DPW Series for 3-D RANS solutions, a systematic study of grid-convergence characteristics of each of the fundamental building blocks of a 3-D RANS CFD method might be required. For example, it may be necessary to study grid-convergence properties for an algorithm on 1-D problems with exact solutions. For the most part, this has already been done extensively in academic settings. However, previous studies conducted on 2-D cases occurred at a time when the limiting factor was computational resources. In addition, 2-D problems receive less investigation than 1-D cases by academia, and less attention than 3-D solutions by industry. This situation is the motivation for the current work [2] presented herein, which focuses on 2-D Euler solutions.

This paper is organized in the following manner. Section II outlines the approach taken in this work to study grid convergence on 2-D Euler flows. Section III provides a description of the subject geometry, which is a slightly modified NACA0012 airfoil. Section IV gives a description of the grid-generation process and the resulting family of grids used for the grid-convergence studies. Section V discusses the estimation of the order of accuracy of a CFD method and the effects on this estimate using data with errors. Section VI provides grid-convergence trends of lift, drag, and pitching moment. Tables of data are embedded within the text, and all figures are appended to the end of the paper.

II. Approach

This section briefly outlines the approach taken in the current work to study grid-convergence properties of various CFD methods on steady-state solutions of 2-D inviscid, compressible flows.

1) The test case is a standard public-domain symmetric airfoil, which is defined by an analytic equation.

2) All numerical calculations are performed with 64-bit computations.

3) All iterative results are converged to machine-level-zero residuals.

4) An extremely high-quality O-mesh is generated about the airfoil. The discrete grid nodes of the piecewise-linear airfoil surface reside on the analytic definition.

5) The O-mesh is composed of essentially orthogonal grid lines and quadrilateral cells of aspect ratio one. Although this class of grid is not necessarily the most efficient use of cell count, nonetheless it is adopted in this work to avoid any issues related to grid stretching or cell aspect ratios.

6) All grids are constructed to be exactly symmetric about the horizontal axis. This permits the possibility of a nonlifting solution at 0 deg angle-of-attack.

7) The cell dimension of the finest grid is selected as a power of 2 to help facilitate construction of a family of grids, as well as to facilitate multigrid acceleration.

8) A family of eight grids is constructed (starting with the finest) by removing every other grid line in both computational directions to create the next coarser grid in the sequence. The coarsest grid used contains 32×32 cells, whereas the finest mesh consists of 4096×4096 elements.

9) Several flow conditions are studied to address different attributes. A zero-lift condition at a subcritical Mach number anchors the study, whereas a heavily investigated transonic flow condition frames the other extreme of this investigation. Two additional conditions are included to provide buildups between the two extremes. The resulting 2×2 matrix of conditions is (subcritical and transonic) by (nonlifting and lifting).

10) Solutions of the 2-D Euler equations are obtained on all grids of the family for each freestream condition under study using FLO82, whereas OVERFLOW and CFL3D solutions have a focus on meshes of dimension 256×256 and larger.

11) Four sets of lifting data are generated using the three CFD methods. Two sets include the influence of a point vortex on the far-field boundary condition, whereas two omit this direct effect. CFL3D is run both ways.

12) The order of accuracy of the CFD methods is estimated using solutions from the three finest meshes of the family. These grid-convergence trends are conducted for all four flow conditions, using all three CFD methods.

13) Estimates are also made for the limiting values of drag, lift, and pitching moment.

14) Note that the drag of an inviscid subcritical flow is precisely zero. This is compared with the estimated limiting values of drag for the subcritical flow conditions to help quantify that the solutions on the finest meshes have indeed reached the asymptotic region of grid convergence for each of the CFD methods.

The next section describes the airfoil geometry under study.

III. NACA0012 Geometry

This section provides a description of the airfoil used in this study. This geometry is a slightly modified NACA0012. A detailed description of this subject geometry is given in Eqs. (1–3). To set the stage for working toward machine-level-zero precision, the values presented in this section are provided to 10 decimal places.

Abbott and von Doenhoff [3] give the analytic equation defining the NACA0012 airfoil. This defining equation and its first and second derivatives are:

$$y(x) = \pm \frac{0.12}{0.2}(0.2969\sqrt{x} - 0.1260x - 0.3516x^2 + 0.2843x^3 - 0.1015x^4) \tag{1}$$

$$y_x(x) = \pm \frac{0.12}{0.2}\left(\frac{0.14845}{\sqrt{x}} - 0.1260 - 0.7032x + 0.8529x^2 - 0.4060x^3\right) \tag{2}$$

$$y_{xx}(x) = \pm \frac{0.12}{0.2}\left(\frac{-0.074225}{\sqrt{x^3}} - 0.7032 + 1.7058x - 1.2180x^2\right) \tag{3}$$

The numerator of the lead terms in Eqs. (1–3), that is, 0.12, is the thickness of the airfoil. The standard NACA0012 airfoil is defined over the interval $0 \le x \le 1$. However, at $x = 1$, the y coordinate does not vanish, and, therefore, the trailing edge (TE) is not sharp, but rather has about a 0.42%-thick blunt base.

To avoid issues related to the solution of inviscid flows about aft-facing steps, the airfoil chord is extended so that the trailing-edge point coincides with the neighboring root of Eq. (1). (Although the actual chord length of this airfoil is slightly greater than one, a reference chord of one is adopted throughout this work to define the nondimensional aerodynamic coefficients of lift, drag, and pitching moment.) The resulting sharp trailing-edge location is

$$x_{\mathrm{TE}} = 1.0089304115 \tag{4}$$

At the sharp trailing-edge location, the slope of the airfoil is

$$y_x(x_{\mathrm{TE}}) = \mp 0.1418768821 \tag{5}$$

Hence, the included angle of the sharp trailing-edge geometry is

$$\tau_{\mathrm{TE}} = 2atan(|y_x(x_{\mathrm{TE}})|) = 0.2818725 \text{ rad} = 16.1501066197 \text{ deg} \tag{6}$$

The included TE angle of Eq. (6) will be needed in the next section to transform the airfoil geometry to a near circle by means of the Karman–Trefftz mapping. Another quantity needed for this transformation is the leading-edge radius of the NACA0012. This value is given by Abbott and von Doenhoff [3] as

$$\rho_{\mathrm{LE}} = 1.1019t^2 = 1.1019(0.12^2) = 0.01586736 \tag{7}$$

For completeness, the location and value of the maximum thickness are also provided. Here $x_{t\max}$ is determined by finding the root of Eq. (3) in the interval $0 \le x \le x_{\mathrm{TE}}$, and $t_{\max} = 2y_{\max}$.

$$x_{t\max} = 0.2998278780 \qquad t_{\max} = 0.1200345462 \tag{8}$$

The next section describes the generation of the grids and the grid family used herein.

IV. Grid Generation and Family of Meshes

This section describes the grid generation adopted for this study. Recall that our approach specified that the mesh be of extremely high quality. To accomplish this the Karman–Trefftz conformal transformation [4] is used, which is defined as

$$\left[\frac{\zeta-\zeta_1}{\zeta-\zeta_2}\right] = \left[\frac{z-z_1}{z-z_2}\right]^P; \qquad P = \left(\frac{\pi}{2\pi-\tau}\right) \tag{9}$$

Here, $z = x + iy$ is the physical plane containing the NACA0012 contour, while $\zeta = \xi + i\eta$ is the mapped plane where the airfoil is transformed to a near circle. The singular points of the transformation are z_1, z_2, and ζ_1, ζ_2, respectively, in the physical and mapped planes; τ is the trailing-edge included angle provided by Eq. (6).

Removing the corner of the trailing edge can be accomplished by placing the first singular point at the sharp trailing edge, and using the correct power of the transformation as defined in Eq. (9). Furthermore, by placing the second singular point at half the leading-edge (LE) radius inside the airfoil contour at the LE, a near circle is obtained in the mapped plane. Hence

$$z_1 = x_{\mathrm{TE}} + i0 = 1.0089304115 \qquad z_2 = \frac{1}{2}\rho_{\mathrm{LE}} + i0 = 0.0079337 \tag{10}$$

Under the transformation of Eq. (9), the singular points of Eq. (10) and the leading-edge point map to the following locations

$$\zeta_1 = 0.77043505 \quad \zeta_2 = 0.24642903 \quad \zeta_{\mathrm{LE}} = 0.20139626 \quad \zeta_{\mathrm{TE}} = \zeta_1 \tag{11}$$

Figure 1 illustrates the Karman–Trefftz transformation, based on Eqs. (1–11), of the NACA0012 airfoil contour to a near circle in the mapped plane. Note that the singular points of this transformation are depicted as symbols in this figure.

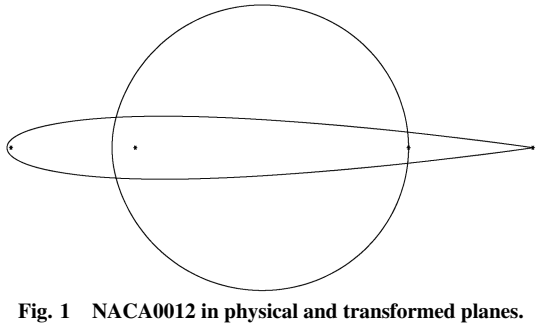

Fig. 1 NACA0012 in physical and transformed planes.

To generate the O-mesh about the near circle contour in the ζ plane, the center of this quasi circle is arbitrarily set as the midpoint of the mapped chordline

$$\zeta_c \equiv \frac{1}{2}(\zeta_{\mathrm{LE}} + \zeta_{\mathrm{TE}}) = 0.4859156 \tag{12}$$

Relative to this center point, the discrete points of the quasi circle are redistributed by linear interpolation with constant angular spacing. Unfortunately, this interpolation in the mapped plane introduces small errors in the airfoil coordinates when transformed back to physical space. To remedy this, the z coordinates are projected back onto the airfoil contour of Eq. (1). This process is repeated until the coordinates in both the z and ζ planes of all geometry points have converged to machine level zero.

With the quasi circle defined by nodes at constant-θ spacing, the field mesh is generated with concentric quasi circles that emanate outward to the far-field boundary. To achieve quadrilateral cells with an aspect ratio of one, the radial spacing must equal the spacing in the angular direction, hence $\Delta r = r\Delta\theta$. If the quasi circle was actually a perfect circle of radius R_1, the radii of the concentric circles can be defined as follows

$$R_j = R_1 e^{\frac{(j-1)2\pi}{NC}}; \qquad 1 \le j \le NC+1 \tag{13}$$

Here, the j subscript signifies the grid index in the computational direction normal to the quasi-circle contour, and NC is the number of cells in the j direction. R_1 is set as the discrete arclength of the quasi circle divided by 2π.

To conform the mesh to the quasi circle at the near-field boundary, a perturbation of the perfect concentric circles of Eq. (13) is introduced

$$r_{i,j} = \frac{r_{i,1}(R_{NC+1} - R_1) + R_{NC+1}(R_j - R_1)}{(R_{NC+1} - R_1)}; \qquad 1 \le i, j \le NC+1 \tag{14}$$

Here, the i subscript signifies the grid index in the angular direction that wraps around the quasi circle. As it turns out, if $j_{\max} = i_{\max}$, the resulting far-field boundary is about 150 chord lengths away from the airfoil surface in the physical plane. In this work $j_{\max} = i_{\max} = NC + 1$ is adopted for all grids.

To ensure that the final grid is exactly symmetric about the x axis, the grid coordinates are processed in the following manner

$$(\hat{x}, \hat{y})_{i,j} = \frac{1}{2}[(x,y)_{i,j} + (x,-y)_{ic,j}]; \qquad 1 \le i \le ile, \qquad 1 \le j \le j\max \tag{15}$$

where $ic = (i\max + 1 - i)$ is the complementary index to i and $ile = (\frac{NC}{2} + 1)$. Then the coordinates of the final grid are replaced with the averaged values of $(\hat{x}, \hat{y})$

$$(x,y)_{i,j} = (\hat{x},\hat{y})_{i,j}, ; \qquad (x,y)_{ic,j} = (\hat{x},-\hat{y})_{i,j}, ; \qquad 1 \le i \le ile, \qquad 1 \le j \le j\max) \tag{16}$$

Figure 2 illustrates the resulting O-mesh in the mapped plane ($NC = 128$) by application of Eqs. (1–14). Applying the inverse of Eq. (1) to this mesh constructs an extremely high-quality O-mesh in the physical plane about the airfoil contour. The first five grids of the family are shown in Figs. 3–8. Figure 8 provides an extreme close-up view of the last 2% of the airfoil with surrounding grid for the (512×512) mesh. In the finest mesh of our family, each cell of the (512×512) mesh is further populated with 64 cells.

The next section discusses several issues related to the estimation of the order of accuracy of a CFD method.

V. Estimating Order of Accuracy

Estimating the order of accuracy of a CFD method has been a topic of ongoing discussion. For example, see Baker [5] and Salas [6].

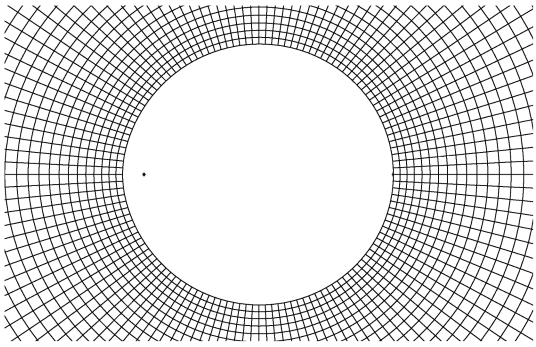

Fig. 2 Closeup of transformed 128 × 128 O-mesh.

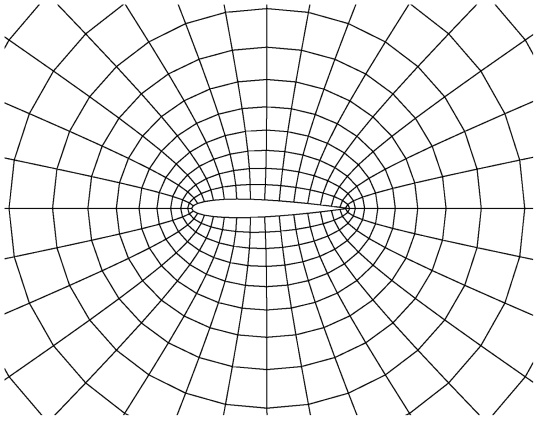

Fig. 3 Closeup of the 32 × 32 O-mesh.

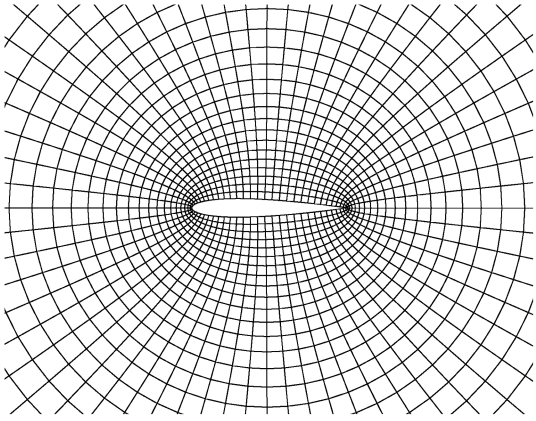

Fig. 4 Closeup of the 64 × 64 O-mesh.

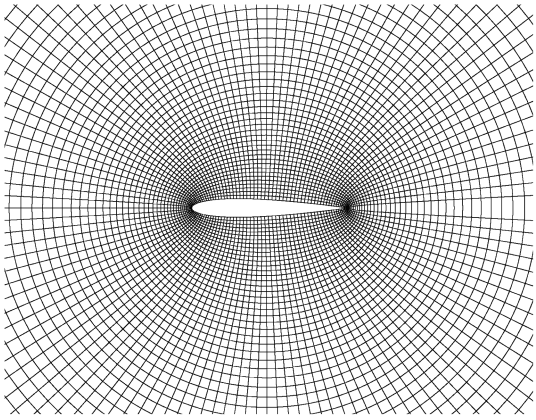

Fig. 5 Closeup of the 128 × 128 O-mesh.

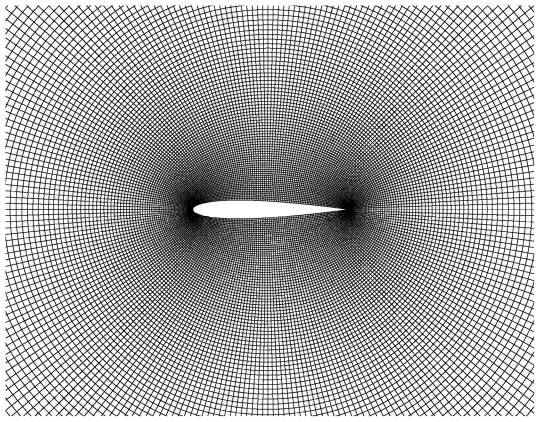

Fig. 6 Closeup of the 256 × 256 O-mesh.

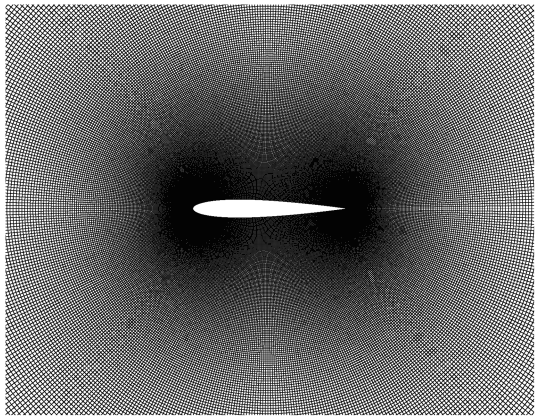

Fig. 7 Closeup of the 512 × 512 O-mesh.

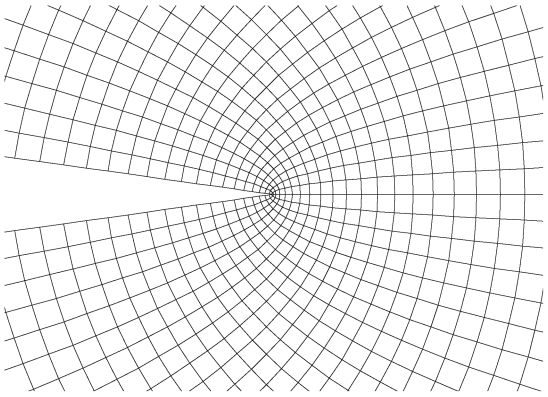

Fig. 8 Extreme closeup of O-mesh near trailing edge.

Following the work of Baker in his analysis of the database generated by the Second Drag Prediction Workshop (DPW-II), we begin our discussion with a generalized equation of computing the order of accuracy

$$(\mathcal{F}_f - \mathcal{F}_m)h_c^p + (\mathcal{F}_c - \mathcal{F}_f)h_m^p + (\mathcal{F}_m - \mathcal{F}_c)h_f^p = 0 \qquad (17)$$

Here, $\mathcal{F}$ is the discrete functional computed on fine, medium, and coarse meshes of a family of grids, signified by subscripts f, m, and c, respectively. The length scale of the cells of a mesh is designated h, and the estimate of the order of accuracy is the power p. Equation (17) requires $h_f < h_m < h_c$. Further, $[\mathcal{F}_c, \quad \mathcal{F}_m, \quad \mathcal{F}_f]$ must be a monotonic sequence.

In the present work, the family of grids has the relation

$$h_c = \omega h_m = \omega^2 h_f = 2h_m = 4h_f \tag{18}$$

Here, $\omega = 2$ is the ratio of cell sizes between grid family levels. Also note that

$$(\mathcal{F}_c - \mathcal{F}_f) = (\mathcal{F}_c - \mathcal{F}_m) + (\mathcal{F}_m - \mathcal{F}_f) \tag{19}$$

Combining Eqs. (17–19) and manipulating gives the following relationship between the ratio of functional changes between meshes $\mathcal{R}$ and an estimate for the order of accuracy p

$$\mathcal{R} = \frac{(\mathcal{F}_f - \mathcal{F}_m)}{(\mathcal{F}_m - \mathcal{F}_c)} = \frac{(\omega^p - 1)}{(\omega^{2p} - \omega^p)} = \frac{(2^p - 1)}{(4^p - 2^p)} \tag{20}$$

If the sequence $[\mathcal{F}_c, \quad \mathcal{F}_m, \quad \mathcal{F}_f]$ is monotonic, then $\mathcal{R} > 0$ and p can be solved. However, if $\mathcal{R} > 1$, the order of accuracy becomes negative.

To solve for p in Eq. (20), let

$$\mathcal{G}(p) = (\omega^{2p} - \omega^p)\mathcal{R} - \omega^p + 1 = (4^p - 2^p)\mathcal{R} - 2^p + 1 = 0 \tag{21}$$

The first derivative of $\mathcal{G}$ with respect to p is

$$\begin{aligned}\mathcal{G}_p(p) &= \ell_n(\omega^2)\omega^{2p}\mathcal{R} - \ell_n(\omega)\omega^p(\mathcal{R} + 1) \\ &= \ln(4)4^p\mathcal{R} - \ln(2)2^p(\mathcal{R} + 1)\end{aligned} \tag{22}$$

Now p from Eq. (20) can be solved for with the Newton method

$$p^{n+1} = p^n - \frac{\mathcal{G}(p^n)}{\mathcal{G}_p(p^n)} \tag{23}$$

where n is the iteration count and $p^0 > p$ always yields a convergent series for $p > 0$.

In the present work, an estimate of the limiting value of $\mathcal{F}$ as $h \to 0$ can then be computed with

$$\mathcal{F}^\star = \mathcal{F}_f + \frac{(\mathcal{F}_f - \mathcal{F}_m)}{(\omega^p - 1)} = \mathcal{F}_f + \frac{(\mathcal{F}_f - \mathcal{F}_m)}{(2^p - 1)} \tag{24}$$

Because drag for any subcritical inviscid flow is identically zero, Eq. (24) can be manipulated to estimate an alternative order of accuracy for drag using only the medium and fine-mesh results. Here $C_d^\star = 0$, and we get

$$\bar{p} = \log_\omega\left[\frac{C_{dm}}{C_{df}}\right] = \log_2\left[\frac{C_{dm}}{C_{df}}\right] \tag{25}$$

Now p from Eqs. (17–23) can be compared with $\bar{p}$ for trends of the subcritical cases to assess how close the CFD data have captured the asymptotic range as well as the physically correct limiting value of drag.

A. Effect of Functional Error on Estimate of Order of Accuracy

The results of Eqs. (23) and (24) assume that the evaluations of the functional in the monotonic sequence $[\mathcal{F}_c, \quad \mathcal{F}_m, \quad \mathcal{F}_f]$ are known exactly. In the state of the practice, however, this is typically not the case; flow solutions are routinely not sufficiently converged to yield a valid outcome. For example, data from the Drag Prediction Workshop Series [1] have been independently reviewed by Baker [5] and Salas [6] with the conclusion that the DPW data are not suitable to establish an estimate on the order of accuracy of the CFD methods used in the workshops. It is for this reason that the organizers of the DPW series plotted the aggregate of the grid-convergence data against a given metric that tends as Δx^2. This decision was made with the understanding that the assumption of second-order accuracy may not be correct, yet is no worse than attempting to solve for p with the uncertainty of the data provided.

To better understand how an error in the discrete function evaluations can affect the estimate on the order of accuracy, let us assume that inaccurate values of $\mathcal{F}$ are given. This approximate value of the discrete functional is then

$$\hat{\mathcal{F}} = \mathcal{F} \pm \epsilon \tag{26}$$

where

$$\epsilon = \beta|\mathcal{F}_f - \mathcal{F}_m| = \beta\mathcal{R}|\mathcal{F}_m - \mathcal{F}_c| \tag{27}$$

Here β is a normalized error parameter that multiplies the delta functionals between the medium and fine meshes to provide the absolute error ϵ. When an error is introduced into the functional $\hat{\mathcal{F}}$, the evaluation of $\mathcal{R}$ in Eq. (20) gives an erroneous result $\hat{\mathcal{R}}$, which can be contaminated to an extent bounded by the range

$$\left[\frac{|\mathcal{F}_f - \mathcal{F}_m| - 2\epsilon}{|\mathcal{F}_m - \mathcal{F}_c| + 2\epsilon}\right] \le \hat{\mathcal{R}} \le \left[\frac{|\mathcal{F}_f - \mathcal{F}_m| + 2\epsilon}{|\mathcal{F}_m - \mathcal{F}_c| - 2\epsilon}\right] \tag{28}$$

Combining Eqs. (26–28) gives

$$\mathcal{R}\left[\frac{(1 - 2\beta)}{(1 + 2\beta\mathcal{R})}\right] \le \hat{\mathcal{R}} \le \mathcal{R}\left[\frac{(1 + 2\beta)}{(1 - 2\beta\mathcal{R})}\right] \tag{29}$$

Figure 9 illustrates the impact of errors in the functionals on the estimation of order of accuracy p. Here, the error bands are depicted with several values of β, specifically $[\frac{1}{16}, \frac{1}{8}, \frac{1}{4}]$. For example, if the error in the functional evaluations is characterized by $\beta = \frac{1}{8}$, then a scheme that is estimated to be first-order accurate may actually be a scheme of order as high as 1.5 or as low as 0.3. Further, note that if $\beta \ge \frac{1}{2}$, the error in the estimate of p is unbounded from below.

To better understand the nature of the impact of functional errors on the estimate on order of accuracy, in the present work let us require that $\beta < \frac{1}{16}$. This requires that the absolute drag must be accurately computed to within an error of $\epsilon < 6 * 10^{-8}$ for the FLO82 subcritical cases; this is six counts-of-a-count in drag. In the DPW databases, which are loosely based on $h_c = 1.5h_m = 2.25h_f$ (ω= 1.5), the effect of β is amplified relative to that indicated by Fig. 9; however, the deltas between the fine and medium meshes are much larger on the 3-D RANS solutions than they are for the 2-D Euler results of this study. Nonetheless, a DPW-class grid-convergence study to accurately estimate order of accuracy would require $\epsilon \ll 0.1$ counts.

To minimize the effect of an inaccurate evaluation of the discrete functionals, all flow solutions of the present work are converged to machine-level-zero steady states using 64-bit computations. Although this standard may be appropriate for the finest grid used in this study, eventually quadruple precision will be required if the grids are refined much further.

Figures 10–12 provide examples of the convergence histories of residuals for FLO82, OVERFLOW, and CFL3D, respectively, for the

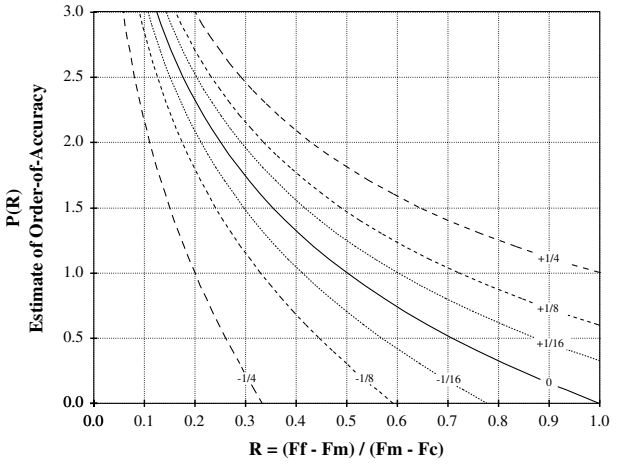

Fig. 9 Effect of discrete-function error on estimate of order of accuracy.

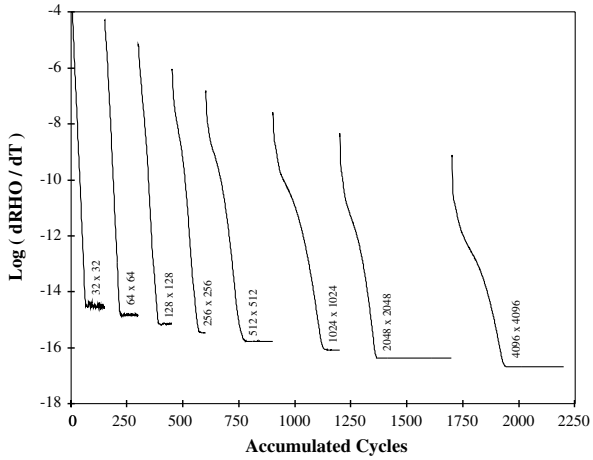

Fig. 10 FLO82 convergence history on all meshes for $M = 0.50$, $\alpha = 1.25$ deg.

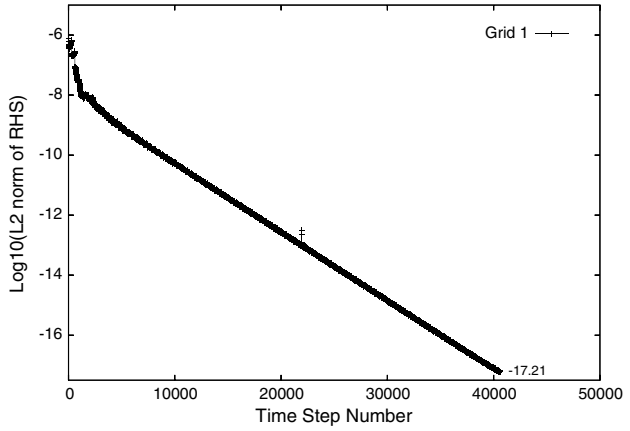

Fig. 11 OVERFLOW convergence history on the finest mesh for $M = 0.50$, $\alpha = 1.25$ deg.

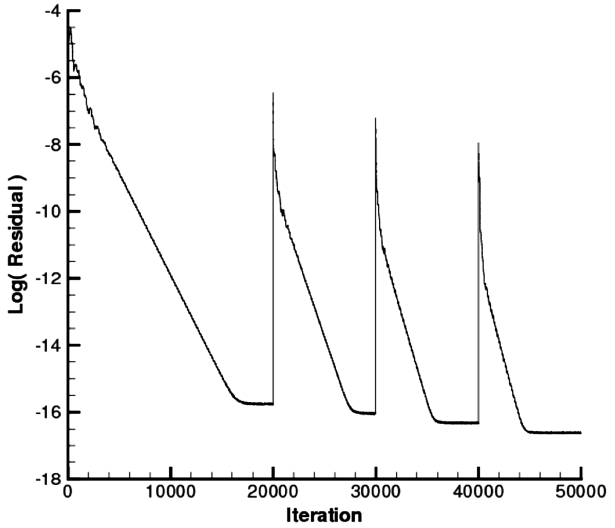

Fig. 12 CFL3D convergence history on four meshes for $M = 0.50$, $\alpha = 1.25$ deg.

subcritical lifting condition of $M = 0.5$, and $\alpha = 1.25$ deg. We note that the convergence rates of the transonic conditions are considerably slower for all three methods, and therefore additional cycles are required to reach equivalently converged solutions.

The next section discusses the results of our study on grid convergence.

VI. Results

This section provides grid-convergence trends for the three CFD methods. The CFD methods are FLO82, OVERFLOW, and CFL3D; their results will be independently discussed in the subsections that follow. At the end of this section, a comparison is made of the continuum estimates of the aerodynamic coefficients for the modified NACA0012 airfoil under study.

Solutions of the 2-D Euler equations for nonlifting and lifting cases at both subcritical and supercritical transonic flow conditions are investigated. The matrix of flow conditions under consideration is provided in Table 1.

The aerodynamic coefficients of lift, drag, and pitching moment are based on a reference chord length of $C_{\text{ref}} = 1.0$ and a moment center of $X_{\text{ref}} = 0.25$.

Figures 13–16 provide the surface pressure distributions and flowfield Mach contours about the modified NACA0012 airfoil for the four flow conditions of Table 1, as computed by FLO82 on the finest mesh of (4096×4096) cells. Mach contours are at intervals of 0.05, and sonic lines (if present) are highlighted in bold. Also provided are minimum and maximum values of local Mach number in the discrete fine-mesh solution.

Figures 13 and 14 depict the subcritical cases of nonlifting and lifting flows, respectively. Note that the maximum local Mach number of these solutions are 0.6198906 and 0.6753743 for the nonlifting and lifting flow conditions, respectively. Recall that the drag of an inviscid subcritical flow is zero.

Similarly, Figs. 15 and 16 depict the transonic cases of nonlifting and lifting flows. The nonlifting case exhibits a fairly strong shock on both surfaces, while the lifting condition is characterized by a very strong shock on the upper surface and a fairly weak shock on the lower surface.

Choice of this set of flow solutions allows the ability to investigate grid-convergence trends of: 1) drag with and without lifting effects (Kutta condition), 2) drag with and without shock effects (upwind stencil), and 3) lift and pitching moment at constant angle of attacks (far-field boundary condition).

The next subsection discusses the results of the FLO82 study.

A. FLO82-H-CUSP Grid-Convergence Study

In this subsection, the grid-convergence characteristics of the FLO82 Euler method [7] are investigated. The upwinding used is the H-CUSP dissipation scheme of Jameson [8]. In addition, FLO82 includes the influence of a point vortex on the far-field boundary condition.

The standard mesh sequencing and multigrid solution process of FLO82 is quite convenient for the purpose of this study. During this process the converged forces and pitching moment at each mesh level are computed. These values, convergence histories, and plots like those of Figs. 13–16 are output at each mesh level. An aggregate of the FLO82 results are tabulated in Tables 2 and 3, for the subcritical and transonic flow conditions, respectively. Note that the $\alpha = 0$ deg cases do not tabulate C_l or C_m, as these quantities are all evaluated as machine-level zero. The data in these tables also include estimates for the order of accuracy for each functional, as well as a Richardson extrapolation of each functional to its limiting value at the continuum where $h = 0$. For the subcritical cases, the alternative estimate of order of accuracy $\bar{p}$ based on Eq. (25) is also provided.

For the subcritical data of Table 2, all aerodynamic coefficients exhibit approximately a second-order-accurate trend, with drag showing slightly less than order 2, while lift and pitching moment indicate slightly better than order 2. Note that $\bar{p}$ is in fairly close agreement with p where applicable. These subcritical results are very promising.

Table 1 Matrix of flow conditions studied

(M, α)	Nonlifting	Lifting
Subcritical	($0.5M$, 0 deg)	($0.5M$, 1.25 deg)
Transonic	($0.8M$, 0 deg)	($0.8M$, 1.25 deg)

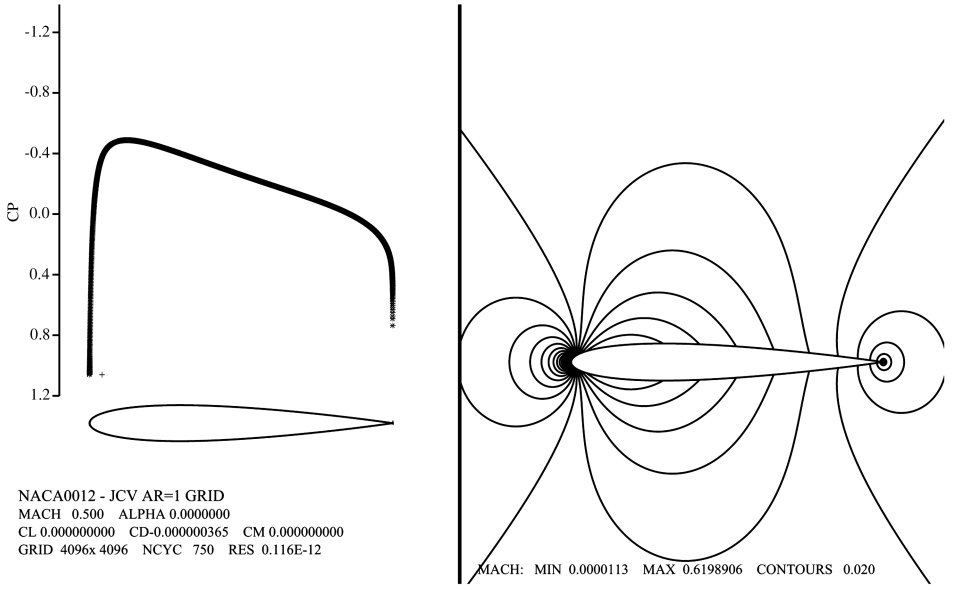

Fig. 13 FLO82 solution $M = 0.50$, $\alpha = 0.0$ deg.

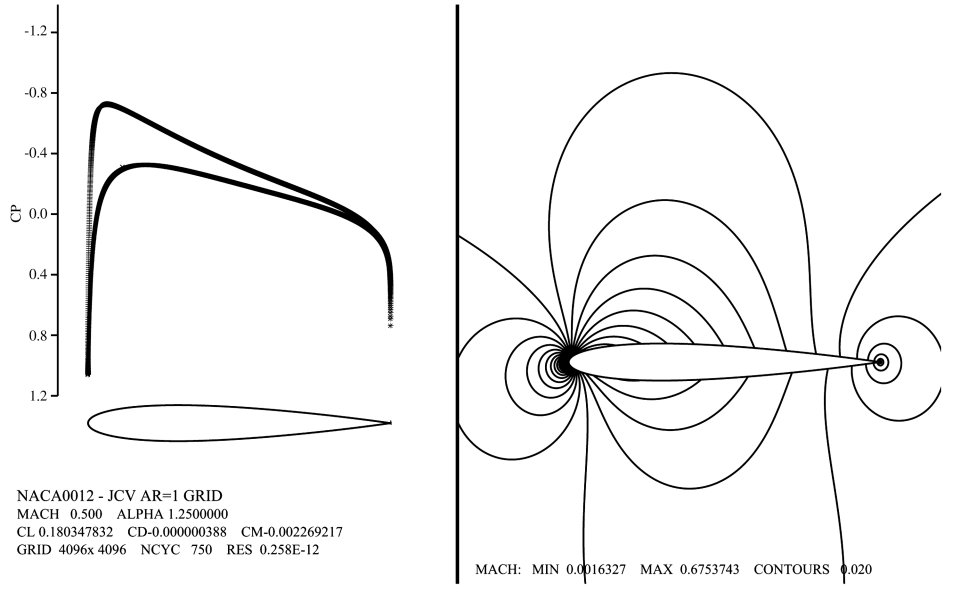

Fig. 14 FLO82 solution $M = 0.50$, $\alpha = 1.25$ deg.

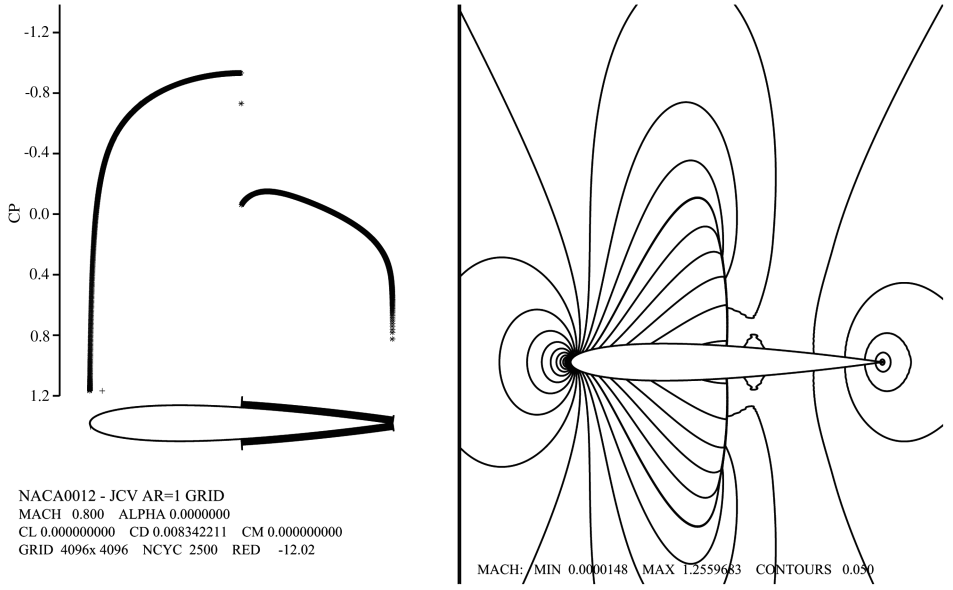

Fig. 15 FLO82 solution $M = 0.80$, $\alpha = 0.0$ deg.

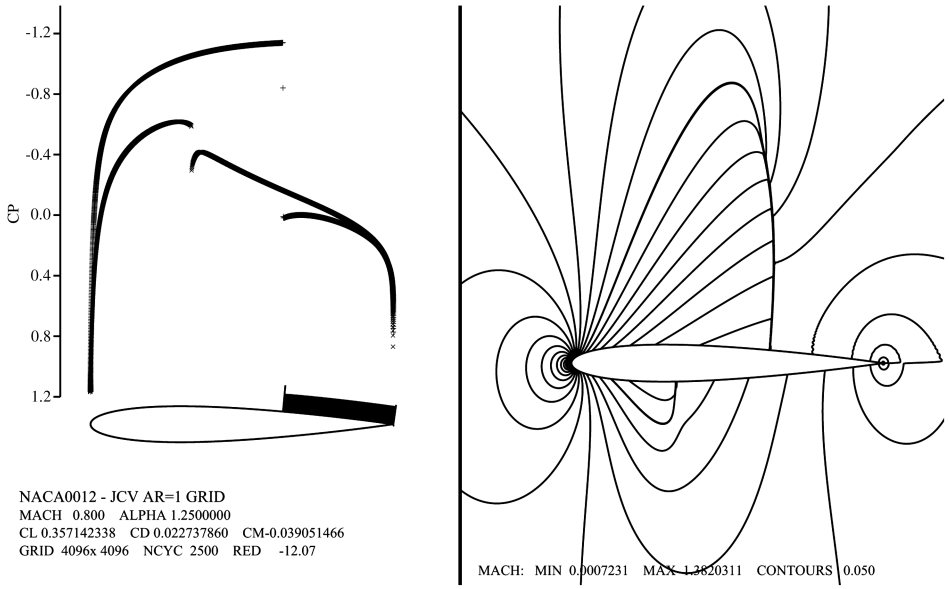

Fig. 16 FLO82 solution $M = 0.80$, $\alpha = 1.25$ deg.

The transonic data of Table 3 illustrate something else altogether. Here, all aerodynamic coefficients for the lifting case exhibit a first-order-accurate character. However, the drag of the nonlifting case shows an unanticipated grid-convergence trend of order $p = 2.631$. This hyper-convergence is not well understood.

The data of Tables 2 and 3 are plotted on a log-log scale in Figs. 17–24. Because these data span the full family of grids, some of the data are not in the asymptotic range. To help visually identify which of these data are clearly outside the asymptotic range, the final monotonic sequence for each case is depicted with solid symbols. Therefore, the open symbols represent data that should not be used to establish grid-convergence metrics. For FLO82, the final monotonic sequence of functionals begin with the 256×256 mesh, but entering the asymptotic range appears to require at least the 512×512 mesh consisting of 262,144 cells.

The next subsection discusses the results of the OVERFLOW study.

B. OVERFLOW(v2.1t) Grid-Convergence Study

In this subsection, the grid-convergence characteristics of the OVERFLOW general-purpose CFD method [9] are investigated. The version of OVERFLOW studied is (2.1t). An initial attempt was made to conduct this study using Roe upwinding. However, the

Table 2 FLO82-H-CUSP subcritical data at $M = 0.5$

Mesh		$\alpha = 0$ deg		$\alpha = 1.25$ deg	
NC	NC^2	C_d	C_l	C_d	C_m
32	1,024	+0.001979418	+0.181639135	+0.002482085	−0.002926241
64	4,096	+0.002270216	+0.178822451	+0.001974608	−0.002487849
128	16,384	+0.000307646	+0.180014345	+0.000298397	−0.002294411
256	65,536	−0.000013299	+0.180458183	−0.000011045	−0.002301404
512	262,144	−0.000015191	+0.180446183	−0.000015534	−0.002290609
1,024	1,048,576	−0.000005076	+0.180382615	−0.000005301	−0.002276577
2,048	4,194,304	−0.000001404	+0.180354386	−0.000001481	−0.002270586
4,096	16,777,216	−0.000000365	+0.180347832	−0.000000388	−0.002269217
Continuum		+0.000000045	+0.180345850	+0.000000050	−0.002268812
Order p		1.821	2.107	1.805	2.130
$\bar{p}$		1.944	——	1.932	——

Table 3 FLO82-HCUSP transonic data at $M = 0.8$

Mesh		$\alpha = 0$ deg		$\alpha = 1.25$ deg	
NC	NC^2	C_d	C_l	C_d	C_m
32	1,024	+0.011451356	+0.387842746	+0.027861593	−0.042947499
64	4,096	+0.010264792	+0.372921380	+0.025487792	−0.043584427
128	16,384	+0.008500758	+0.373469550	+0.023786371	−0.043873739
256	65,536	+0.008312402	+0.368980205	+0.023357651	−0.042552941
512	262,144	+0.008328328	+0.363747900	+0.023084749	−0.041002228
1,024	1,048,576	+0.008338967	+0.360812844	+0.022934404	−0.040136414
2,048	4,194,304	+0.008341760	+0.358281928	+0.022799839	−0.039388829
4,096	16,777,216	+0.008342211	+0.357142338	+0.022737860	−0.039051466
Continuum		+0.008342298	+0.356208937	+0.022684938	−0.038774022
Order p		2.631	1.151	1.118	1.148

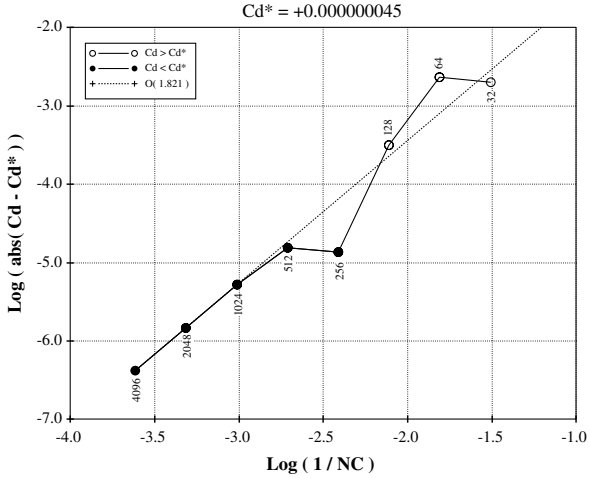

Fig. 17 FLO82 drag convergence $M = 0.50$, $\alpha = 0.0$ deg.

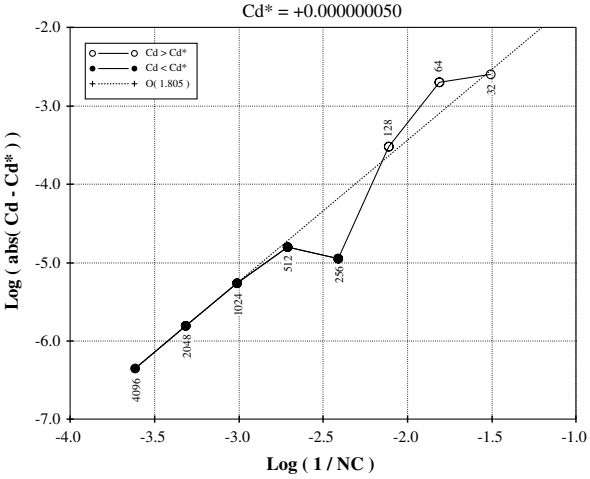

Fig. 18 FLO82 drag convergence $M = 0.50$, $\alpha = 1.25$ deg.

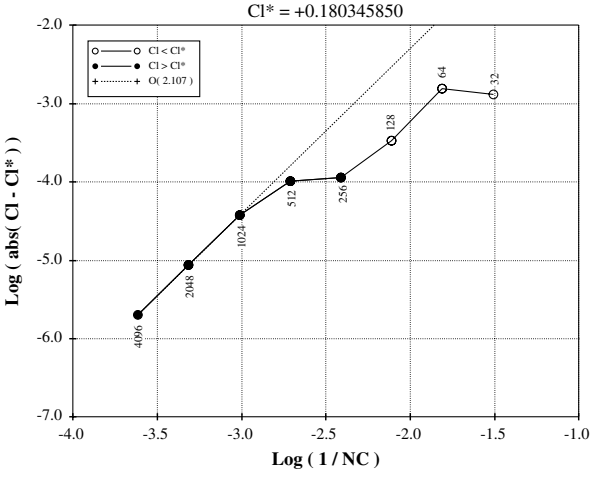

Fig. 19 FLO82 lift convergence $M = 0.50$, $\alpha = 1.25$ deg.

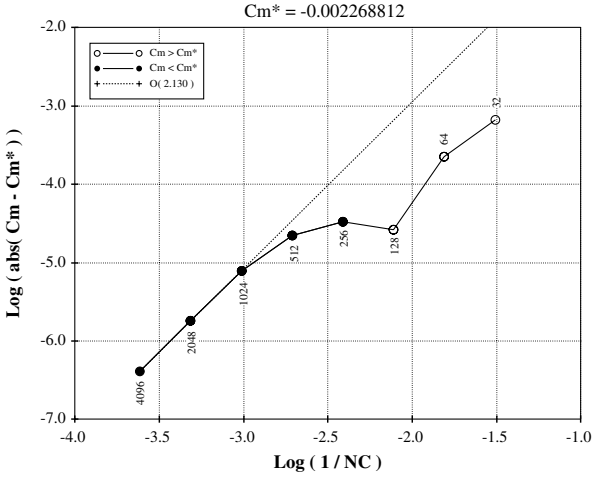

Fig. 20 FLO82 C_m convergence $M = 0.50$, $\alpha = 1.25$ deg.

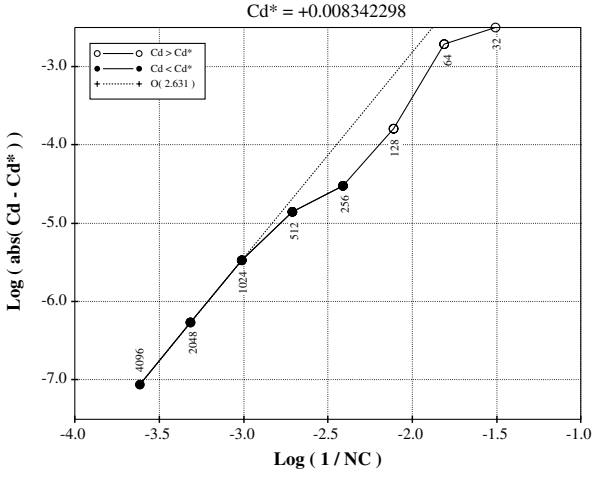

Fig. 21 FLO82 drag convergence $M = 0.80$, $\alpha = 0.0$ deg.

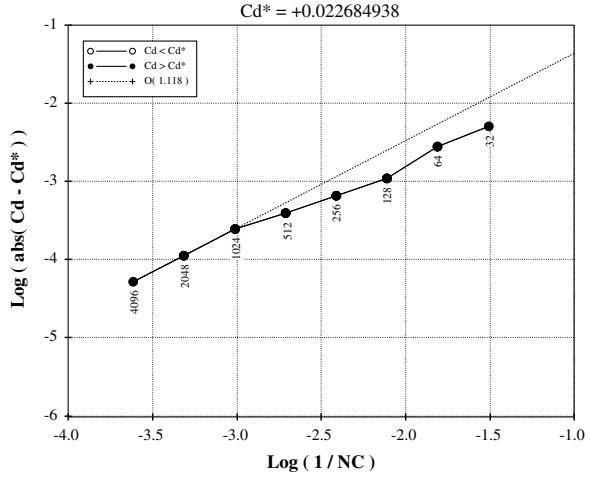

Fig. 22 FLO82 drag convergence $M = 0.80$, $\alpha = 1.25$ deg.

convergence of residuals stalled at values far above machine-level zero. As a consequence, we decided to use the central-differencing scheme with all of the artificial-dissipation parameters set to their recommended default values. The pressure boundary condition imposed at the airfoil surface is based on the momentum equation ($IBTYP = 2$) and a Riemann-invariant boundary condition was used at the far field ($IBTYP = 47$). This far-field boundary condition does not carry the direct influence of the point vortex.

Because the previous study indicates that the coarsest three mesh levels are clearly outside the asymptotic range for FLO82, we focus our efforts here on the top five meshes of the full family. Solutions for each mesh and flow condition are started from scratch and converged to machine-level zero. To be consistent across the family of meshes,

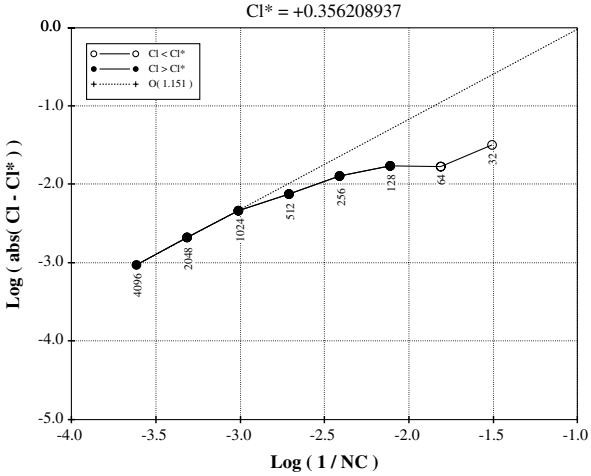

Fig. 23 FLO82 lift convergence $M = 0.80, \alpha = 1.25$ deg.

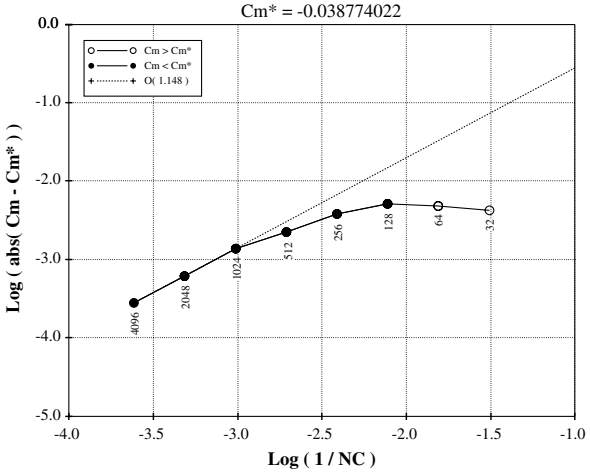

Fig. 24 FLO82 C_m convergence $M = 0.80, \alpha = 1.25$ deg.

all of the cases are run in parallel on 64 processors. The results of this study are tabulated in Tables 4 and 5 for the subcritical and transonic flow conditions, respectively. As before, the nonlifting cases all yield machine-level-zero coefficients of lift and pitching moment.

For the subcritical data of Table 5, all aerodynamic coefficients exhibit no better than a first-order-accurate trend. Most troubling is the nonlifting case, which yields an order of accuracy of $p = 0.691$, and an estimate of drag at the continuum of about 4% of a count. Furthermore, $\bar{p}$ and p do not agree well with each other where applicable.

The transonic data of Table 7 provide some interesting results. Here, the order of accuracy for drag on the nonlifting case has increased to first order as compared with that of the subcritical nonlifting condition. In contrast, the transonic lifting cases exhibit lower order of accuracies than the corresponding subcritical results.

The data of Tables 4 and 5 are plotted on a log–log scale in Figs. 25–32. All of these data monotonically vary with increasing mesh dimension. In every case, the four finest meshes of the series fall on the asymptotic slope, and even the coarsest mesh of 256×256 is close to doing the same for many of the cases.

The next subsection discusses the results of the CFL3D study.

C. CFL3D(v6) Grid-Convergence Study

In this subsection, the grid-convergence characteristics of the CFL3D general-purpose CFD method [10,11] are investigated. The version of CFL3D studied is (v6). Two far-field boundary conditions ($i2d = \pm 1$) are considered for the lifting cases of this study. One far-field boundary condition includes the effect of a point vortex and the other does not. An initial attempt was made to conduct this study using Roe upwinding. However, as with OVERFLOW, the convergence of residuals stalled at values well above machine-level zero. As a consequence, the flux-spitting scheme of CFL3D was used instead. Some of the pertinent input parameters are $ifds[i, j, k] = 0$, $rkap0[i, j, k] = \frac{1}{3}$. All solutions were run in parallel on 64 processors. Unfortunately, this setup would not provide machine-level-zero results for the 4096×4096 mesh without resorting to CFL $= -1$, which required too much elapsed time for the current work. Therefore, the data provided for CFL3D exclude this finest mesh. As it turns out, the four mesh levels of data obtained reasonably indicate that the asymptotic range of CFL3D has been captured. The results of this study are tabulated in Tables 6–9 for the subcritical and transonic

Table 4 OVERFLOW-central subcritical data at $M = 0.5$

Mesh		$\alpha = 0$ deg		$\alpha = 1.25$ deg	
NC	NC^2	C_d	C_l	C_d	C_m
256	65,536	+0.000063743	+0.178960502	+0.000118671	−0.002124907
512	262,144	+0.000044712	+0.179435775	+0.000068207	−0.002191480
1,024	1,048,576	+0.000028691	+0.179627329	+0.000044071	−0.002226157
2,048	4,194,304	+0.000016232	+0.179710209	+0.000029311	−0.002243944
4,096	16,777,216	+0.000008512	+0.179747254	+0.000020951	−0.002253042
Continuum		−0.000004058	+0.179777193	+0.000010030	−0.002262569
Order p		0.691	1.162	0.820	0.967
$\bar{p}$		0.931	——	0.484	——

Table 5 OVERFLOW-central transonic data at $M = 0.8$

Mesh		$\alpha = 0$ deg		$\alpha = 1.25$ deg	
NC	NC^2	C_d	C_l	C_d	C_m
256	65,536	+0.008734038	+0.353909135	+0.022964252	−0.038987812
512	262,144	+0.008493959	+0.353798330	+0.022706732	−0.038656831
1,024	1,048,576	+0.008412129	+0.353241712	+0.022593342	−0.038402691
2,048	4,194,304	+0.008376064	+0.352827907	+0.022534646	−0.038251571
4,096	16,777,216	+0.008358591	+0.352522552	+0.022500576	−0.038150471
Continuum		+0.008342171	+0.351662793	+0.022453440	−0.037946129
Order p		1.046	0.438	0.785	0.580

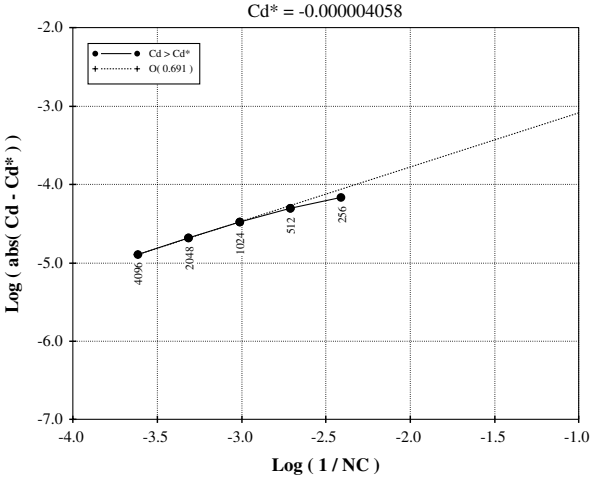

Fig. 25 Overflow drag convergence $M = 0.50$, $\alpha = 0.0$ deg.

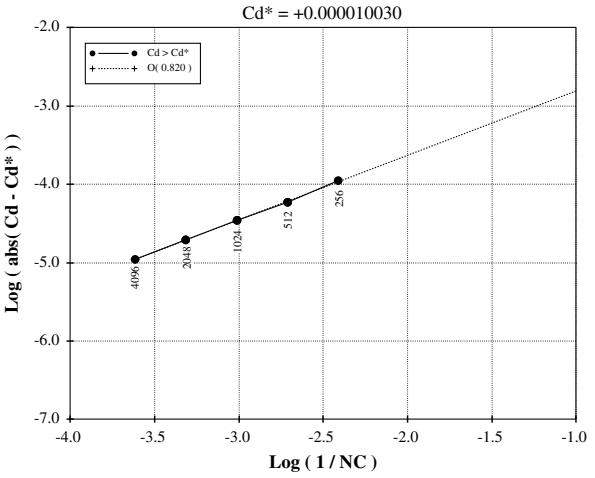

Fig. 26 Overflow drag convergence $M = 0.50$, $\alpha = 1.25$ deg.

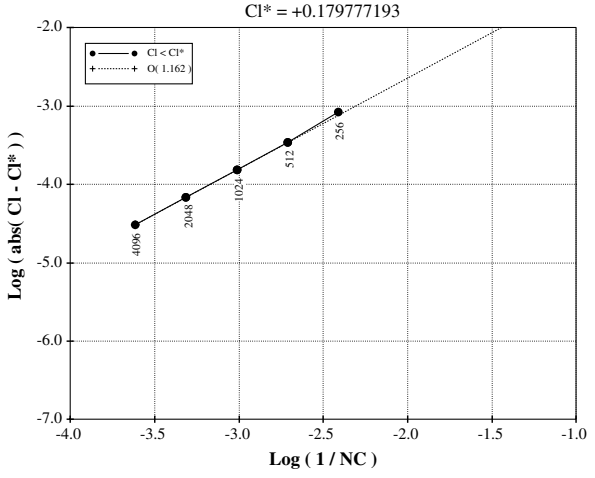

Fig. 27 Overflow lift convergence $M = 0.50$, $\alpha = 1.25$ deg.

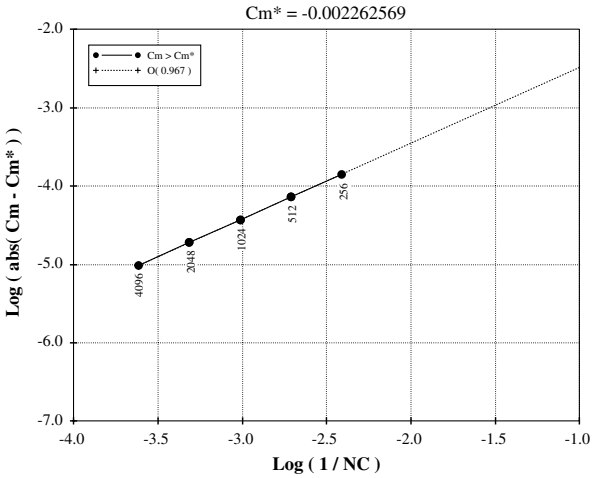

Fig. 28 Overflow C_m convergence $M = 0.50$, $\alpha = 1.25$ deg.

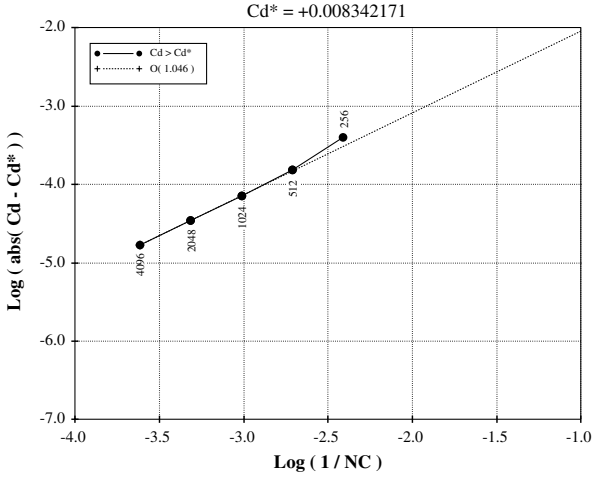

Fig. 29 Overflow drag convergence $M = 0.80$, $\alpha = 0.0$ deg.

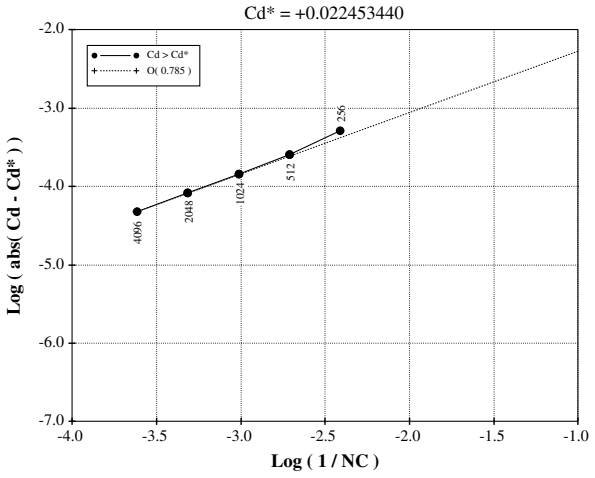

Fig. 30 Overflow drag convergence $M = 0.80$, $\alpha = 1.25$ deg.

flow conditions, respectively. As before, the nonlifting cases all yielded machine-level-zero coefficients of lift and pitching moment.

For the subcritical data of Tables 6 and 7, a curious trend emerges for CFL3D's order-of-accuracy assessments. Specifically, it is second-order accurate for drag, but only first-order accurate for lift and pitching moment. This is true for the nonlifting case, the lifting case without point vortex, and the lifting case with the point-vortex influence on the far-field boundary condition. However, $\bar{p}$ and p do not agree well with each other for the lifting case without the influence of the point vortex.

The transonic data of Tables 8 and 9 show that the drag for the nonlifting case retains a second-order-accurate trend, but drops to

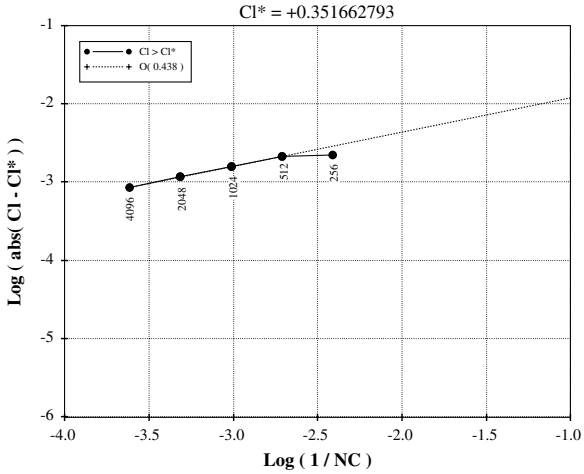

Fig. 31 Overflow lift convergence $M = 0.80$, $\alpha = 1.25°$.

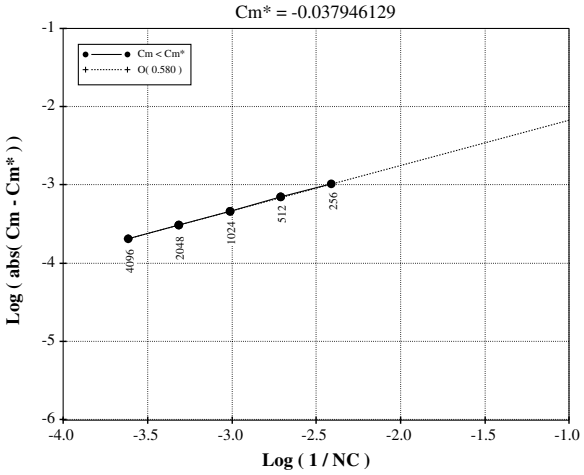

Fig. 32 Overflow C_m convergence $M = 0.80$, $\alpha = 1.25°$.

first order for both sets of lifting data. The data for lift and pitching moment yield very low estimates on order of accuracy in the $\frac{1}{4}\frac{1}{3}$ range.

The data of Tables 6–9 are plotted on a log–log scale in Figs. 33–40. All of these data monotonically vary with increasing mesh dimension. In nearly every case, the 256×256 data fall on the trend line established by the three finer meshes of the family studied here. Even though results for the 4906×4096 mesh could not be obtained in time for this printing, it appears that the asymptotic range of CFL3D has been captured with the meshes used.

The next subsection compares the estimates of the continuum values as predicted by the three CFD methods under study.

D. Summary of Continuum Estimates

In this subsection, we compare the limiting values of the aerodynamic coefficients by extrapolating the data of the three CFD methods to the continuum. These limiting values are provided in Tables 10 and 11 for the subcritical and transonic flow conditions, respectively. Also included are their minimum, maximum, and spread values.

For the subcritical cases of Table 10, the limiting values of drag from FLO82 results are very close to zero; this is true for both the nonlifting and lifting cases. The drag from CFL3D also estimates a limiting value close to zero for the nonlifting case, and for the lifting case based on the point-vortex far-field boundary condition. However, the drag from CFL3D without the point vortex is considerably larger, by almost two orders of magnitude. OVERFLOW predicts the largest drag for the nonlifting case of about 0.04 counts, and this increases to about 0.1 counts when lifting. The total spread between the three CFD methods on lift is about 3% and about 2% on pitching moment; these results are somewhat discouraging for a subcritical flow.

In Table 11, the case of nonlifting transonic flow has all three methods agreeing quite closely on the limiting value of drag, coming in around $C_d = 0.0083419$. For the lifting case, the spread on drag is about 1%, on lift about 2%, and about 3% for pitching moment. Interestingly, these differences are no worse than those of the subcritical flows. Nevertheless, they are worse than we would like to see.

Table 6 CFL3D-flux-splitting subcritical data at $M = 0.5$

Mesh		$\alpha = 0$ deg	$\alpha = 1.25$ deg		
NC	NC^2	C_d	C_l	C_d	C_m
256	65,536	+0.000573147	+0.178366720	+0.000649962	−0.002078508
512	262,144	+0.000131328	+0.179125033	+0.000163415	−0.002152971
1,024	1,048,576	+0.000031615	+0.179487608	+0.000048451	−0.002206480
2,048	4,194,304	+0.000007502	+0.179650543	+0.000020903	−0.002235646
Continuum		−0.000000192	+0.179783519	+0.000012221	−0.002270588
Order p		2.048	1.154	2.061	0.876
$\bar{p}$		2.075	——	1.213	——

Table 7 CFL3D-flux-splitting and vortex subcritical data at $M = 0.5$

Mesh		$\alpha = 1.25$ deg		
NC	NC^2	C_l	C_d	C_m
256	65,536	+0.178919799	+0.000638328	−0.002084517
512	262,144	+0.179686024	+0.000151327	−0.002159318
1,024	1,048,576	+0.180052519	+0.000036185	−0.002213043
2,048	4,194,304	+0.180217309	+0.000008575	−0.002242320
Continuum		+0.180351940	−0.000000134	−0.002277383
Order p		1.153	2.060	0.876
$\bar{p}$		——	2.077	——

Table 8 CFL3D-flux-splitting transonic data at $M = 0.8$

Mesh		$\alpha = 0$ deg	$\alpha = 1.25$ deg		
NC	NC^2	C_d	C_l	C_d	C_m
256	65,536	+0.008894250	+0.359073197	+0.023411409	−0.040316445
512	262,144	+0.008479528	+0.357580694	+0.022902709	−0.039700797
1,024	1,048,576	+0.008376058	+0.355943711	+0.022706750	−0.039170890
2,048	4,194,304	+0.008350161	+0.354593186	+0.022606485	−0.038760613
Continuum		+0.008341516	+0.348226045	+0.022501430	−0.037353559
Order p		1.998	0.278	0.967	0.369

Table 9 CFL3D-flux-splitting and vortex transonic data at $M = 0.8$

Mesh		$\alpha = 1.25$ deg		
NC	NC^2	C_l	C_d	C_m
256	65,536	+0.362292941	+0.023590480	−0.040813294
512	262,144	+0.360850141	+0.023082744	−0.040205152
1,024	1,048,576	+0.359172468	+0.022884500	−0.039664060
2,048	4,194,304	+0.357798948	+0.022782607	−0.039246655
Continuum		+0.351596613	+0.022674853	−0.037838046
Order p		0.289	0.960	0.374

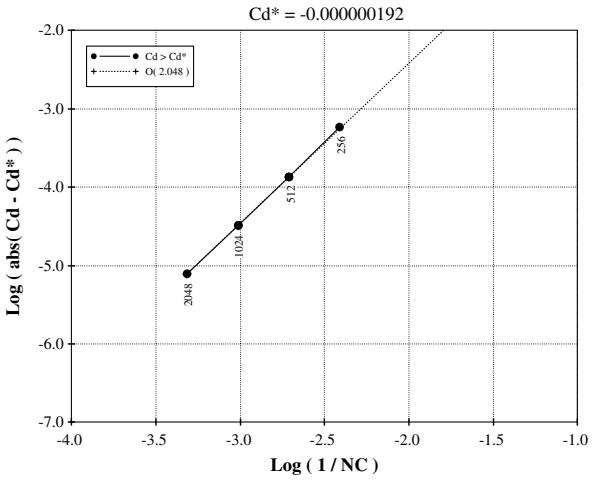

Fig. 33 CFL3D drag convergence $M = 0.50$, $\alpha = 0.0$ deg.

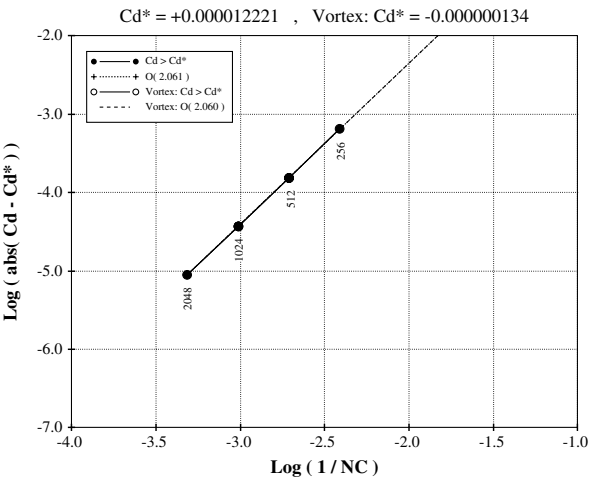

Fig. 34 CFL3D drag convergence $M = 0.50$, $\alpha = 1.25$ deg.

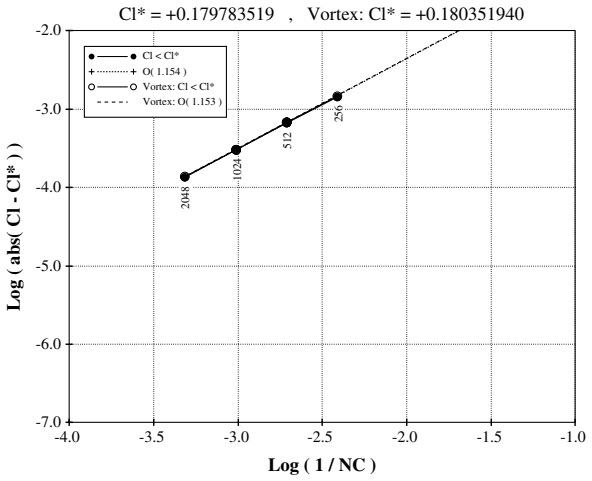

Fig. 35 CFL3D lift convergence $M = 0.50$, $\alpha = 1.25$ deg.

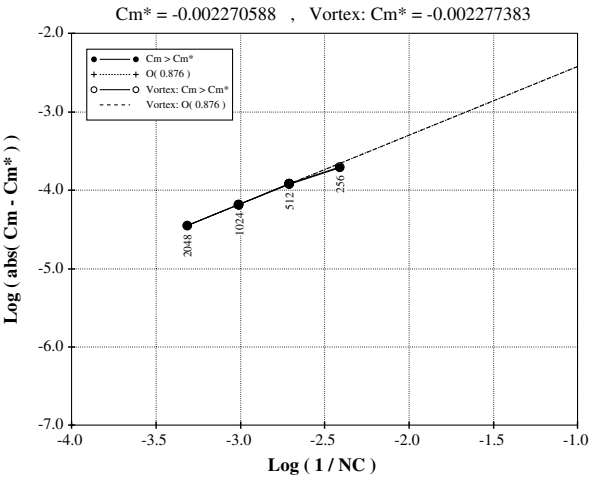

Fig. 36 CFL3D C_m convergence $M = 0.50$, $\alpha = 1.25$ deg.

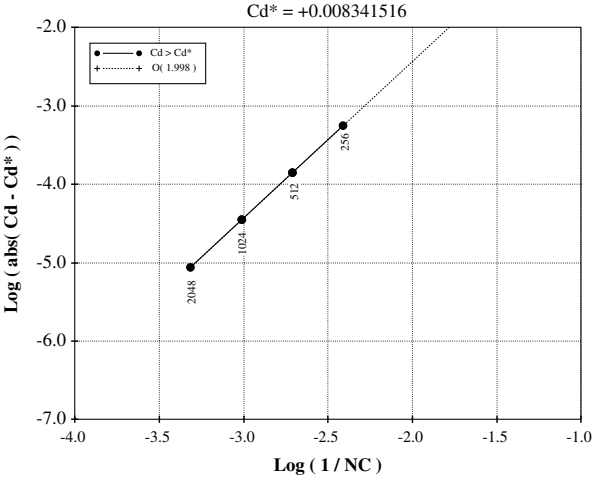

Fig. 37 CFL3D drag convergence $M = 0.80$, $\alpha = 0.0$ deg.

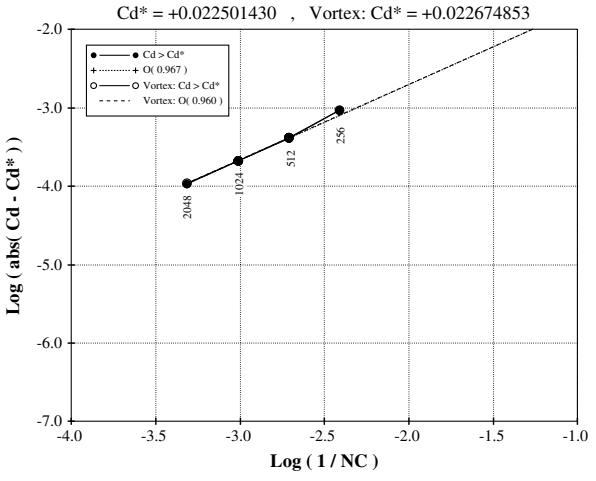

Fig. 38 CFL3D drag convergence $M = 0.80$, $\alpha = 1.25$ deg.

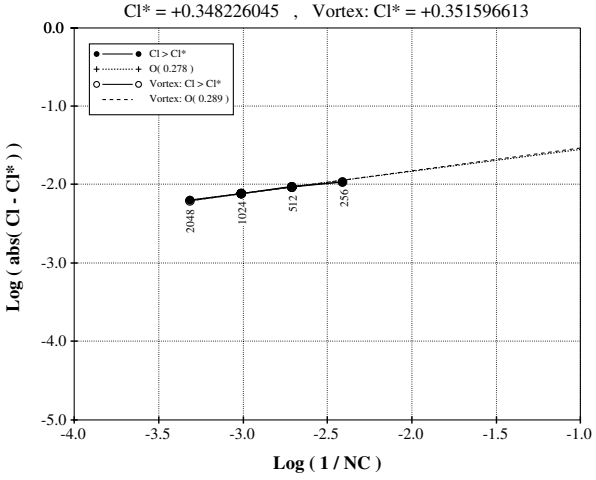

Fig. 39 CFL3D lift convergence $M = 0.80$, $\alpha = 1.25$ deg.

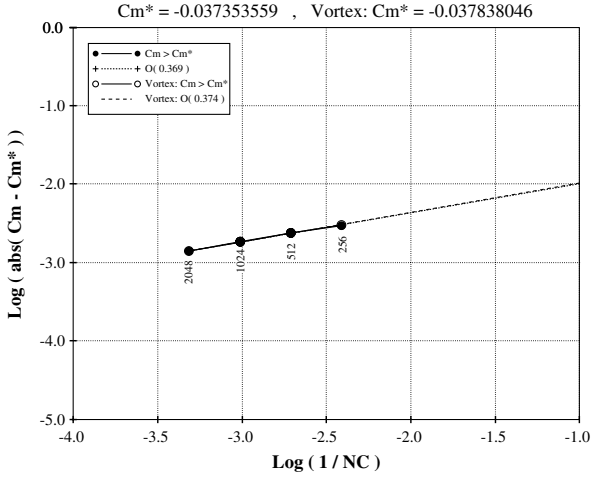

Fig. 40 CFL3D C_m Convergence $M = 0.80$, $\alpha = 1.25$ deg.

Table 10 Comparison of continuum estimates at $M = 0.5$

$M = 0.5$	$\alpha = 0$ deg		$\alpha = 1.25$ deg	
CFD Method	C_d	C_l	C_d	C_m
FLO82	+0.000000045	+0.180345850	+0.000000050	−0.002268812
OVERFLOW v2.1t	−0.000004058	+0.179777193	+0.000010030	−0.002262569
CFL3Dv6	−0.000000192	+0.179783519	+0.000012221	−0.002270588
CFL3Dv6 + Vortex	-	+0.180351940	−0.000000134	−0.002277383
Min	−0.000004058	+0.179777193	−0.000000134	−0.002277383
Max	+0.000000045	+0.180351940	+0.000012221	−0.002262569
Spread	0.000004103	0.000574747	0.000012355	0.000014814

Table 11 Comparison of continuum estimates at $M = 0.8$

$M = 0.8$	$\alpha = 0$ deg		$\alpha = 1.25$ deg	
CFD Method	C_d	C_l	C_d	C_m
FLO82	+0.008342298	+0.356208937	+0.022684938	−0.038774022
OVERFLOW v2.1t	+0.008342171	+0.351662793	+0.022453440	−0.037946129
CFL3Dv6	+0.008341516	+0.348226045	+0.022501430	−0.037353559
CFL3Dv6 + Vortex	-	+0.351596613	+0.022674853	−0.037838046
Min	+0.008341516	+0.348226045	+0.022453440	−0.038774022
Max	+0.008342298	+0.356208937	+0.022684938	−0.037353559
Spread	0.000000782	0.007983097	0.000231508	0.001420422

VII. Conclusions

Grid-convergence trends of two-dimensional Euler solutions are investigated. The airfoil geometry under study is based on the NACA0012 equation; however, it is extended in chord to yield a sharp trailing edge. The flow solutions use extremely high-quality grids, which are developed with the aid of the Karman–Trefftz conformal transformation. The topology of each grid is that of a standard O-mesh. The grids extend to a far-field boundary approximately 150 chord lengths away from the airfoil. Each quadrilateral cell of the resulting mesh has an aspect ratio of one, and the intersecting grid lines are essentially orthogonal at each vertex within the mesh. A family of grids is derived from the finest mesh, whereas each successively coarser grid in the sequence is constructed by eliminating every other node, in both computational directions. In all, a total of eight grids comprise the family, with the coarsest-to-finest meshes having dimensions of 32×32–4096×4096 cells, respectively. The finest grid in this family is composed of over 16 million cells, and is suitable for 13 levels of multigrid. The geometry and grids are all defined such that they are exactly symmetrical about the horizontal axis to ensure that a nonlifting solution is possible at 0 deg angle-of-attack attitude.

Issues related to estimating the order of accuracy of a CFD method are discussed. These include the effect of errors introduced into the discrete functionals, which may arise due to insufficiently converged flow solutions. It is possible to determine the maximum allowable error that provides an assessment to the order of accuracy to a desired tolerance. Based on this error analysis, quadruple precision will eventually be required if the grid family of the present study is extended to include finer meshes.

Characteristics of three well-known flow solvers (FLO82, OVERFLOW, and CFL3D) are studied using a matrix of four flow conditions: (subcritical and transonic) by (nonlifting and lifting). The matrix allows the ability to investigate grid-convergence trends of 1) drag with and without lifting effects, 2) drag with and without shocks, and 3 lift and moment at constant angle of attacks. The asymptotic range of FLO82 appears to begin with the 512×512 mesh, whereas the asymptotic ranges of OVERFLOW and CFL3D seem to begin with the 256×256 mesh. Second-order-accurate trend lines are demonstrated on the subcritical flow conditions for FLO82 and CFL3D. For the transonic nonlifting condition, FLO82 and CFL3D continue to show second-order accuracy. However, for the transonic lifting case, both CFD methods drop to first order. The order of accuracy for OVERFLOW at all flow conditions is at best first order.

Four sets of subcritical lifting data from the three CFD methods are provided: FLO82 with the influence of a point vortex on the far-field boundary, OVERFLOW without it, and CFL3D with and without this effect. It is interesting to note that the solution sets that include the point vortex yield limiting values of drag that are much closer to zero than do the solution sets that omit the point-vortex effect.

The asymptotic behavior of the flow solution near the singular point of the trailing edge could impact the accuracy of the numerical integrations of the forces and pitching moment. This and other issues will be addressed in our ongoing work in pursuit of grid convergence.

References

[1] 4th AIAA CFD Drag Prediction Workshop, San Antonio, TX, June 2009.

[2] Vassberg, J. C., and Jameson, A., "In Pursuit of Grid Convergence, Part I: Two Dimensional Euler Solutions," AIAA Paper 2009-4114, Reston, VA, June 2009.

[3] Abbott, I. H., and von Doenhoff, A. E., *Theory of Wing Sections*, Dover, New York, 1959, ISBN 0-486-60586-8.

[4] Milne–Thomson, L. M., *Theoretical Aerodynamics*, Dover, New York, 1958, ISBN 0-486-61980-X.

[5] Baker, T. J., "Mesh generation: Art or science?," *Progress in Aerospace Sciences*, Vol. 41, No. 1, 2005, pp. 29–63. doi:10.1016/j.paerosci.2005.02.002

[6] Salas, M. D., "Digital Flight: The Last CFD Aeronautical Grand Challenge," *Journal of Scientific Computing*, Vol. 28, Nos. 2–3, Sept. 2006, pp. 479–505. doi:10.1007/s10915-006-9087-7

[7] Jameson, A., "Solution of the Euler Equations for Two Dimensional Transonic Flow by a Multigrid Method," *Applied Mathematics and Computation*, Vol. 13, Nos. 3–4, 1983, pp. 327–356. doi:10.1016/0096-3003(83)90019-X

[8] Jameson, A., "Artificial Diffusion, Upwind Biasing, Limiters and Their Effect on Accuracy and Multigrid Convergence in Transonic and Hypersonic Flows," *AIAA 11th Computational Fluid Dynamics Conference*, AIAA Paper 93–3359, Reston, VA, July 1993.

[9] Nichols, R. H., and Buning, P. G., "OVERFLOW User's Manual Ver. 2.1t.," Univ. of Alabama and NASA, Aug. 2008.

[10] Krist, S. L., Biedron, R. T., and Rumsey, C. L., "CFL3D User's Manual," NASA NASA-TM 1998-208444, June 1998. Version 5.0.

[11] CFL3D Ver. 6.4. http://cfl3d.larc.nasa.gov/Cfl3dv6/cfl3dv6.html, 2006.